

Tunable snapshot imaging spectrometer

Christopher P. Tebow, Eustace L. Dereniak,
Optical Sciences Center, University of Arizona, Tucson, AZ 85721
Dennis Garrood, Raytheon Missile Systems, Tucson, AZ
Terry A. Dorschner, Raytheon Network Centric Systems, Lexington, MA
Curtis E. Volin, Georgia Tech Research Institute, Atlanta, GA

*ctebow@u.arizona.edu; phone 520 626 5600; fax 520 621 9104; <http://www.optics.arizona.edu/detlab>; Optical Sciences Center
Optical Detection Lab, 1630 E. University Blvd, Tucson, AZ, USA 85721

ABSTRACT

The acquisition of a multi-spectral data set in a single FPA integration time (snapshot) with no moving parts or scanning is possible with a Computed Tomographic Imaging Spectrometer (CTIS). CTIS instruments employ specially designed computer generated holograms (CGH) etched in an appropriate media for the wavelength band of interest as the dispersing element. The replacement of current etched CGHs with an electronically tunable liquid crystal Optical Phase Array (OPA) extends the capabilities of the CTIS by adding the ability to change its configuration while maintaining its basic motivation as a non-scanning imaging spectrometer with no moving parts. This tunability allows the dispersion, number of diffraction orders, and diffraction efficiency of the orders to be changed affecting the instrument's spectral resolution, data cube reconstruction quality and speed. This publication presents the results of characterizing the OPA phase vs. applied voltage profile and the feedback algorithm used to program the OPA as a CTIS disperser.

1. INTRODUCTION

Imaging spectrometry has been demonstrated to be a powerful tool in remote sensing applications since the mid-1980's.¹ Traditional dispersive imaging spectrometers collect (x, y, λ) image cube data (see Figure 1) by employing some form of scanning, such as pushbroom scanning (for example, the Hyperspectral Digital Imagery Collection Experiment) or whiskbroom scanning (for example, the Airborne Visible/Infrared Imaging Spectrometer).^{2,3} Alternatively, imaging Fourier transform spectrometers equipped with a focal-plane array (FPA) at the output require scanning of the optical path difference between the two arms of a Michelson interferometer before the image cube can be retrieved from the raw data. Although these methods of data collection are acceptable for stationary or nearly stationary scenes, scanned imaging of dynamic scenes results in artifacts. In the cases of pushbroom or whiskbroom scanning imaging spectrometers, scene motion causes spatial artifacts. In the case of spectrally multiplexing spectrometers, scene motion results in spectral-signature artifacts. The application of computed tomography (CT) in imaging spectrometry is an effective scheme for overcoming these difficulties and for accomplishing instantaneous or flash spectral imaging.⁴ The objective of flash spectral imaging is the acquisition of spatial and spectral information about a scene within the shortest possible data-collection time. Imaging applications that call for this form of data acquisition can be found in astronomy, medicine, industrial testing, and defense.

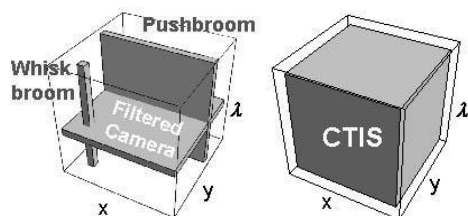


Figure 1a: Example of the datacube collection process with a scanning system (left) and with the CTIS (right)

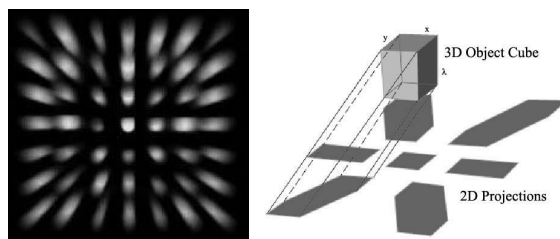


Figure 1b: Raw image collected by a CTIS instrument (left), shadow sketch showing the projections associated with an object cube (right)

High-signal-to-noise-ratio, high-speed imaging of dynamic events can be accomplished only by a nonscanning imaging spectrometer that maximizes the dwell time at each $(\Delta x, \Delta y, \Delta \lambda)$ image-cube resolution element. Current CTIS instruments use a computer-generated hologram (CGH) disperser inserted into the collimated beam between lenses that image a system field-stop onto a large-format FPA. The CGH disperser forms a rectangular array of spectrally dispersed images, each of which can be interpreted as a 2D projection of the three-dimensional (x, y, λ) image cube (see Figure 1b). Based on such an interpretation, it is possible to reconstruct the (x, y, λ) image cube from its 2D projections by employing CT algorithms.

The connection between CT and imaging spectrometry was explored first by Okamoto^{5,6} and Bulygin,⁷ and later its theoretical and practical limitations were defined by Descour and Dereniak.^{4,8} The theoretical limitations may be addressed by a variety of reconstruction constraints, such as positivity or compact support.⁹ The practical limitations are related to the radiative throughput of the instrument and, specifically, to the dispersive element.

This particular computed-tomography imaging spectrometer (CTIS) operates over the 450-720 nm spectral range. The spectrometer consists of three optical-element groups: an image-forming optic, a collimating optic, and a reimaging lens. Figure 2a shows a schematic of the instrument and Figure 2b shows an image of the actual instrument. At left is the objective lens, which images a scene to the field stop. Zoom lenses are used for the collimating and reimaging lenses which allows us to vary the magnification of the field-stop on the FPA. This variation can be used to adjust the effective dispersion within each order.^{8,10} The CGH is placed in collimated space between the collimating and reimaging lenses.

Tunability of the dispersive element allows for the possibility of optical preprocessing of the image, which may significantly lower the computing time needed for reconstructions of data cubes from projections. Specifically, the spectral resolution can change by varying the disperser period, the number of diffraction orders (CT projections) can be changed, and to some degree the spectral diffraction efficiencies of the orders can be changed.

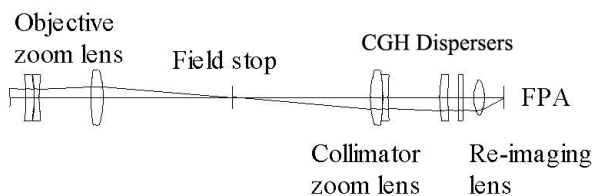


Figure 2a: Schematic of the CTIS

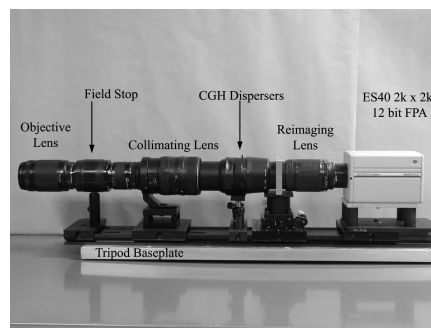


Figure 2b: Image of the CTIS Instrument

2. CGH PHYSICAL LAYOUT

Previous versions of the CTIS have all used a CGH designed as a 2D pixellated phase profile pattern without restriction on the number of usable phase values.^{11,13} Typically the desired efficiencies are such that a 5 x 5 or a 7 x 7 grid of diffraction orders give a uniform irradiance when integrated over wavelength. Higher orders start to overlap as well as fall off the FPA, and are thus designed to have very low diffraction efficiencies. The composition of the CGH is an array of replicated unit cells covering the clear aperture of the disperser. The unit cell is a 2D pixellated phase profile pattern usually of 8 x 8, 10 x 10, or 16 x 16 elements, hereby denoted as 'phasels' (phase elements) to differentiate them from FPA 'pixels'. The mathematical description of the transmission of the entire CGH is¹¹,

$$t(x_1, y_1) \propto \sum_{m,n=0}^{q-1} e^{j\Phi_{mn}} \text{rect}\left(\frac{x_1 - mx_c}{x_c}\right) \text{rect}\left(\frac{y_1 - ny_c}{y_c}\right) ** \sum_{k,l=-\infty}^{\infty} \delta\left(\frac{x_1 - kqx_c}{qx_c}\right) \delta\left(\frac{y_1 - lqy_c}{qy_c}\right) \quad (1)$$

where Φ_{mn} are the pixellated phase profile values, (x_1, y_1) are the coordinates in the plane of the CGH, (x_c, y_c) are the real width and height of each pixel, and the $**$ operator indicates the 2D convolution. Notice that the equation above describes an element that has a unit cell that is replicated many times such that the (k, l) limits in the second summation are set to infinity, and the number of pixels in the unit cell is q^2 . The complex amplitude in the image plane according to the Fraunhofer diffraction model is then the Fourier transform of Equation (1) evaluated at $\xi = x/\lambda f, \eta = y/\lambda f$:

$$E(x, y) \propto \sum e^{j\Phi_{mn}} e^{-j\frac{2\pi}{\lambda f}(mx_c x + ny_c y)} \times \sum \delta\left(x - \frac{k\lambda f}{qx_c}\right) \delta\left(y - \frac{l\lambda f}{qy_c}\right) \times \text{sinc}\left(\frac{x_c x}{\lambda f}\right) \text{sinc}\left(\frac{y_c y}{\lambda f}\right) \quad (2)$$

The sinc functions above are defined as $\text{sinc}(ax)/ax$. The irradiance is the modulus squared of the complex amplitude, and we can see that the point spread function of the CGH will be an array of sinc modulated delta functions with separations inversely proportional to the unit cell size. Figure 3a shows a typical CGH design with $q = 8, k = 0$ to 1 , and $l = 0$ to 1 (four replicated unit cells). Previous CGHs fabricated for University of Arizona CTIS instruments are surface relief elements that are electron beam written in poly-(methyl methacrylate), PMMA, at JPL.

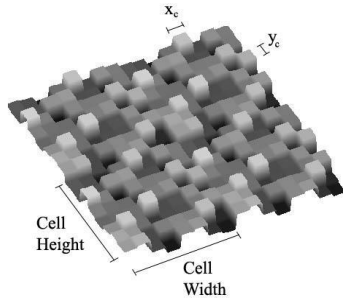


Figure 3a: Surface profile of a CGH disperser

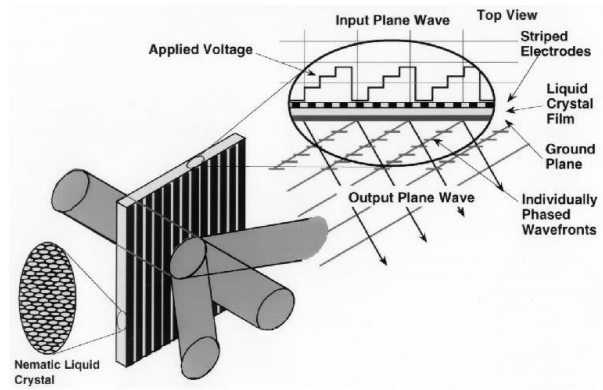


Figure 3b: Schematic of the proposed LC SLM

Tunability requires changing the Φ_{mn} values of the CGH with reasonable speed. Liquid Crystal Spatial Light Modulators (LC SLMs) allow for fairly rapid, programmable tunability of the phase values. However, LC SLMs have limitations in phasel size and the number of independently addressable phasels. For integration with a CTIS instrument, LC SLMs also need completely polarized light to avoid washing out the desired far-field pattern with light from the non-optimal polarization orientations.

Raytheon Network Centric Systems has constructed a LC SLM, alternatively called an Optical Phased Array (OPA), consisting of two sets of crossed, 1-dimensional arrays.¹² The two sets are 'coarse' and 'fine', referring to beam deviation capability, with electrode widths (pitch) of 1 μm and 80 μm , respectively. Only the coarse, with its 2 μm effective pitch (1 μm wide electrodes with 1 μm wide spacings), was used for this project. The OPA uses changes in index with applied voltage to the nematic LC to effect the phase profile rather than etching a surface relief pattern. A sketch of one of the LC cells is shown in Figure 3b. There are 256 independently addressable electrodes that are

$$\begin{aligned} t(x_1, y_1) &\propto \sum_{n=0}^{q-1} e^{j\Phi_n} \text{rect}\left(\frac{x_1 - nx_c}{x_c}\right) \text{rect}\left(\frac{y_1}{Nqy_c}\right) * \sum_{k=0}^{N-1} \delta\left(\frac{x_1 - kqx_c}{qx_c}\right) \\ t(x_2, y_2) &\propto \sum_{n=0}^{q-1} e^{j\Phi_n} \text{rect}\left(\frac{y_2 - ny_c}{y_c}\right) \text{rect}\left(\frac{x_2}{Nqx_c}\right) * \sum_{k=0}^{N-1} \delta\left(\frac{y_2 - kqy_c}{qy_c}\right) \\ t(x, y) &= t(x_1, y_1) \times t(x_2, y_2) \end{aligned} \quad (3)$$

repeated over a 4 cm clear aperture in each of the two crossed LC cells. For visible wavelengths there is roughly 4π radians of 10 bit quantized phase delay available. The transmissions of the crossed coarse LC cells multiply; and the resulting irradiance pattern will be the convolution of the two 1-dimensional irradiance patterns.

3. USING THE RAYTHEON OPA AS A CGH

The goal of the CTIS disperser is to effect a phase profile in the instrument's collimated space resulting in a desired irradiance pattern on the FPA. The way in which the current etched CGH technology and the OPA realize this phase profile differ significantly. The major differences are: (1) the birefringent nature of the OPA necessitating a linear polarizer in the CTIS, (2) the non-linear phase vs. applied voltage of the OPA, and (3) 'flyback' in the OPA, which is a type of inter-electrode crosstalk between the linear phasels. If the phase vs. applied voltage profile is known, it would be possible to design the desired phase pattern for the OPA using the same algorithms as the etched CGHs in the absence of flyback. However, there is no model of the flyback as it applies to CTIS dispersers, and as we shall see this necessitates the use of a feedback algorithm to design the CGH plane (the OPA) based on the detected irradiance pattern.

3.1 Binary Phase Grating

The first step in using the OPA as a CGH is to obtain the phase vs. applied voltage curve. A couple of methods to determine the curve are to use a common path interferometer or a laser based Fizeau, or to program a binary phase grating to the OPA and record the far-field irradiance. Conveniently, the current CTIS calibration method needs only minor changes to perform a binary phase experiment with the OPA. The calibration of the CTIS acquires a set of spectral/spatial point-spread functions (PSFs) by recording the CTIS response when the exit face of a fiber is imaged to the CTIS field stop. The fibers typically used are patch cords from Ocean Optics (100 μm – 600 μm core diameters) fed by light imaged to the fiber's entrance face from the exit port of a grating monochromator. The light source for the monochromator is a tungsten-halogen bulb. The image of the fiber approximates a spatial/spectral 'delta' function. For the binary phase experiment, this same set-up gives plane waves in the OPA plane and the far-field irradiance is the Fourier transform of the OPA's phase profile. The procedure was performed using the LC cell with vertical electrodes while holding the other crossed cell at a constant voltage level across its entire aperture, so this is a 1D binary phase grating. Due to flyback, it is unlikely that the actual linear phase profile is a true rectangle wave, but a rectangle-like profile with roll off at the edges of the phase transition to the other phase level. The widest possible grating period, 256 electrodes, was chosen to minimize this effect.

Theoretically, the zero order efficiency follows a $\eta_0(\phi) = \cos^2(\phi)$ curve when plotted with increasing phase between the two levels of the binary grating. All the odd harmonics follow $\eta(\phi) = A \sin^2(\phi)$ curve, where η is the efficiency and A is close to 0.41 for the first orders and decreases for higher orders. The even harmonics do not exist for the ideal binary phase as they fall on the zeros of the sinc function from the Fourier transform. Figure 4c below shows the results of the relative efficiencies of the first positive and negative eight orders from the experiment. The highest amplitude

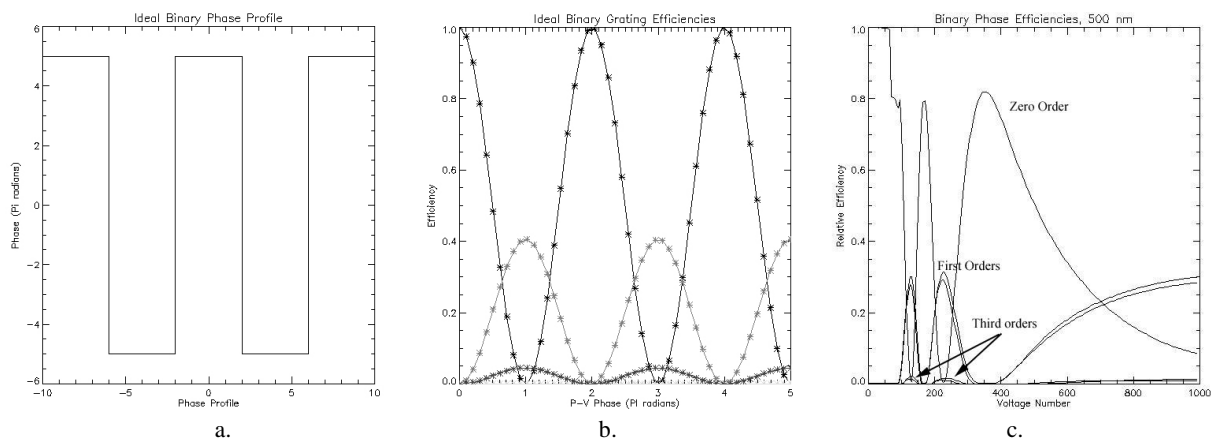


Figure 4: Efficiency vs. applied voltage for the binary phase experiment. The wavelength is 500 nm and the grating period is 256 electrodes.

curve is the zero order, the next highest pair of curves are the positive and negative first orders, and the small ‘humps’ in phase with the first orders are the positive and negative third orders. As expected, only the odd harmonics have any appreciable efficiency. The definition of the relative efficiency used here is the fraction of light in each order with respect to the total light detected in all the orders on the array. The voltage is applied to the OPA via a D/A converter with a 10 bit range (1024 levels), so the x-axis of the plot is labeled ‘Voltage Number’ referring to one of the 1024 levels. Figures 4a and 4b show the ideal binary phase grating profile at a phase delay of 5π radians and the theoretical far-field efficiencies as a function of phase delay.

The major difference between the ideal and experimental binary grating efficiencies (Figure 4b and Figure 4c) is the compression and expansion of the \cos^2 function due to the non-linear relationship between applied voltage and phase in the OPA. Also the maximum efficiency of the zero order does not go back to 1.0 as expected for voltage values corresponding to integer phase delays of π , nor do the first orders peak at 41% efficiency. The major reasons for this are first the flyback and also possibly because of etalon effects due to the coatings of the OPA being optimized for 1.06 μm light. The experiment was performed at 5 different wavelengths, 500, 550, 600, 650, and 700 nm, each at all possible 8 periods (2, 4, 8, 16, 32, 64, 128, and 256 electrodes). Shown in Figure 4c is the result at 500 nm for a 256 electrode period.

Given the results in Figure 4c and ignoring the apparent efficiency loss due to flyback and etalon effects, we can calculate from the data the phase vs. applied voltage profile using the simple equations:

$$\begin{aligned}\eta_0 &= \cos^2(\phi(V)) \\ \phi(V) &= \cos^{-1}(\sqrt{\eta_0})\end{aligned}\quad (4)$$

where η_0 is the efficiency of the zero order and $\phi(V)$ is the phase as a function of quantized voltage. Figure 5a shows the resulting phase vs. voltage plot for the data taken in Figure 4c. It is assumed that the phase vs. voltage profile simply scales with wavelength, and Figure 5b. shows a plot of the phase vs. voltage profiles of all 5 wavelengths at the 256 electrode period scaled to the center wavelength, 600 nm.

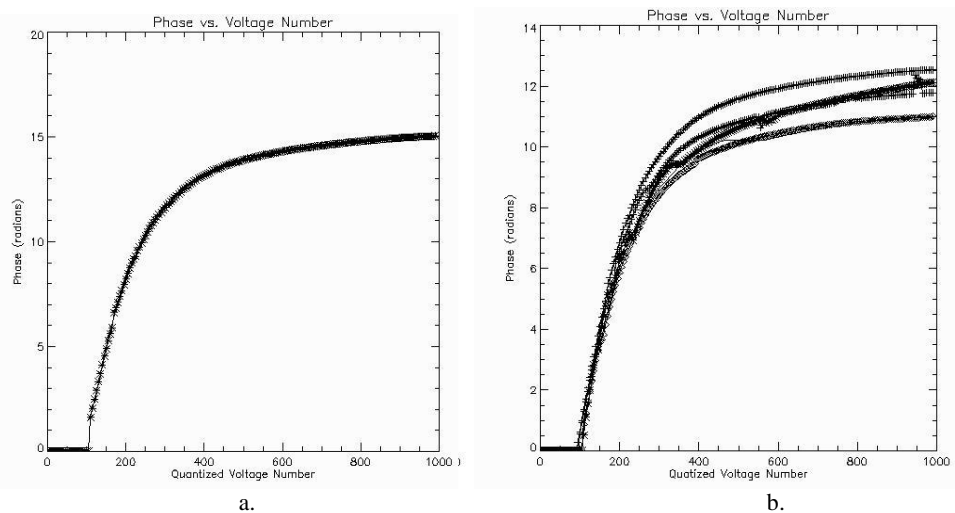


Figure 5: (a) The phase vs. voltage profile for 500 nm and a 256 electrode period. (b) The phase vs. voltage profile of all wavelengths scaled to match the values at 600 nm.

The changing index of the LC has a very sharp cut-on around voltage number 100. Most of the dynamic range is between this cut-on and voltage number 400 at which point the index change is ‘saturated’ as most of the LC molecules are oriented along the opposite axis from their original position. It is assumed that the relationship between quantized voltage number and actual applied voltage is linear. This exercise has proven very useful as it negates the assumption

that the phase response of the OPA simply scales with wavelength. At this time it is unknown why this is, though perhaps the most likely culprit is the previously mentioned etalon effects due to the AR coatings of the OPA.

The procedure above works fairly well at a particular wavelength for the largest period possible with the OPA. However, for application in the CTIS we need just the opposite, the smallest period possible. Current CGHs have periods corresponding to 16 OPA electrodes (32 μm grating pitch), typically with 8, 10, or 16 phasels in each period. As mentioned above, the binary phase experiment was performed at all the possible periods, and Figure 6a-d show the results at 500 nm for periods of 2, 8, 32, and 256 electrodes. The discontinuities in the plots are due to errors in the data acquisition process. Using a binary phase pattern to deduce the phase vs. voltage profile is not valid for periods less than 32 electrodes, and we must use some other method of determining the correct voltages to apply to obtain the desired far-field pattern.

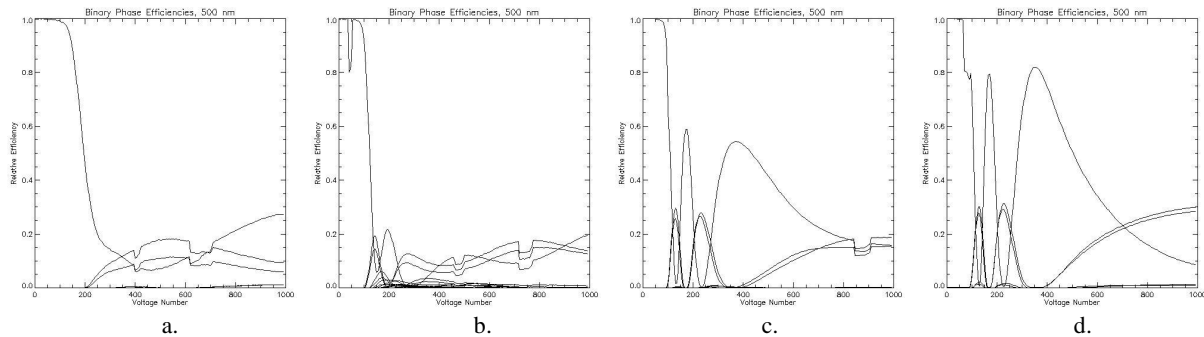


Figure 6 a-d: Diffraction efficiency plots for a binary phase grating with periods of (a) 2 electrodes, (b) 8 electrodes, (c) 32 electrodes, and (d) 256 electrodes.

3.2 Simulated Annealing

One of the more straightforward CGH design methods to apply with the OPA is simulated annealing.¹⁴ The simulated annealing algorithm works by randomly selecting an OPA electrode and changing its voltage level some amount. The resulting far-field irradiance is detected by the camera and the efficiencies of the diffraction orders are calculated. The merit function of the algorithm is the squared error between the weights of the diffraction efficiencies in the desired irradiance pattern and the actual, detected efficiencies:

$$\text{error} = \frac{\sum_{i=-q}^q \left(\frac{\eta_i^{\text{detected}}}{s} - \eta_i^{\text{target}} \right)^2}{\sum_{i=1}^q (\eta_i^{\text{target}})^2} \quad (5)$$

$$s = \frac{\sum_{i=-q}^q (\eta_i^{\text{detected}} \eta_i^{\text{target}})}{\sum_{i=-q}^q (\eta_i^{\text{target}})^2}$$

where q is the number of orders and 's' is the scaling factor between the desired weights and the detected efficiencies. Changes that reduce the squared error between the detected and desired irradiance patterns are kept, while changes that increase the squared error are kept with a probability determined by a Boltzmann distribution, $P(x) = e^{-x/kT}$, which changes according to an annealing schedule. The particular implementation of simulated annealing used here is performed in 1D again using the LC cell with vertical electrodes while holding the other cell to a constant voltage level. The algorithm itself has two parts. For a 16 electrode period, 16000 iterations (average of 1000 perturbations per electrode) were performed using the method described above. The second part is a carbon copy of the first except only changes *reducing* the squared error between the actual and desired irradiances were kept. To speed the algorithm, only a

5 frame average from the camera was used with a set threshold to eliminate noise rather than a dark frame subtraction. The average iteration speed to change the OPA, find the correct camera integration time, and acquire the data with the CTIS camera was 2 seconds. The major drawback of the algorithm is its 15 hour run-time for optimization at a single wavelength. To gain perspective, current CGH algorithms¹¹ take merely hundreds of iterations to find a multi-chromatic solution in 2D in less than an hour, but the design must be then submitted for fabrication using a reactive ion etch (MWIR) or an overnight electron beam write (visible), and then shipped back to the lab. The design, fabrication, and error budget for a CTIS disperser with the OPA are all accomplished with a single, 15 hour run of simulated annealing.

Figure 7a shows the weights of the efficiencies for a 1D disperser for use in the CTIS. Simulated annealing was performed for optimization at 540 nm as described above. The resulting efficiencies are shown in Figure 7b and the squared error versus iteration number (for changes that were kept) is shown in Figure 7c.

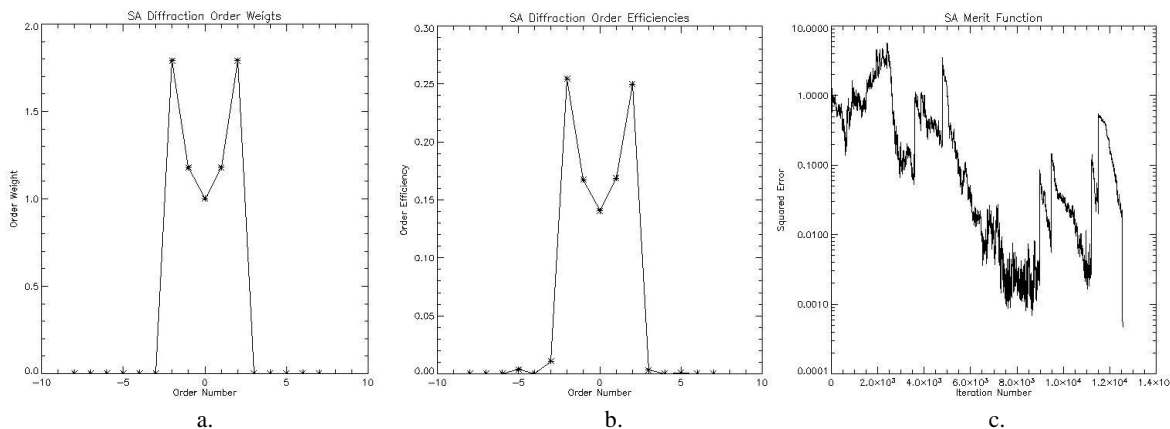


Figure 7 a-c: The target irradiance weights (η^{target}), final diffraction order efficiencies (η^{detected}), and the squared error, respectively

The weights of the pattern are chosen to maximize the dynamic range of the CTIS by putting more light in the higher orders to counteract the loss of light energy per FPA pixel due to higher dispersion. The OPA performs very well at the design wavelength, with over 98% *relative* efficiency in the desired five orders.

Current CTIS dispersers are designed to operate over an entire spectral range, typically with λ_{min} to λ_{max} being one octave. A direct comparison of the broadband performance of the OPA with the current CGH technology is possible using a pair of 1D dispersers that were fabricated at JPL to show the feasibility of using an OPA as a CTIS disperser. The center wavelength for the design is the same as the OPA of Figure 7, 540 nm, and used the same weights as shown in Figure 7a. The algorithm used to design the etched CGHs, however, was a polychromatic SVD algorithm,¹³ and not simulated annealing. The phasel pitch of these test PMMA CGHs are 2.5 μm with 16 phasels per CGH cell for a 40 μm grating period. This closely corresponds with the simulated annealing CGH design of the OPA above which uses 16

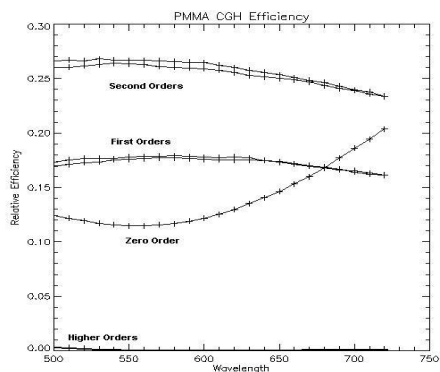


Figure 8a: Relative diffraction efficiency vs. λ for the test PMMA gratings. Only the central 5 orders have appreciable efficiency

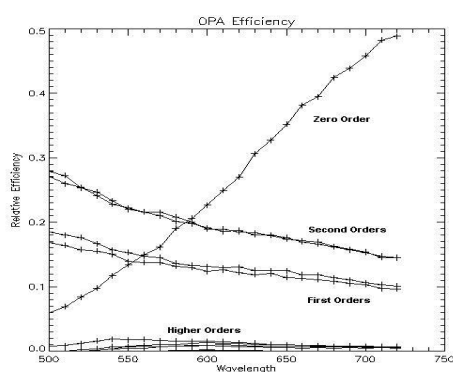


Figure 8b: Relative diffraction efficiencies vs. λ for the OPA. Again, only the central 5 orders have appreciable efficiency.

electrodes per period, each with a 2 μm effective pitch resulting in a 32 μm grating period. The relative diffraction efficiencies as a function of wavelength for the test PMMA CGHs are shown below in Figure 8a, and the relative efficiencies as a function of wavelength for the OPA using the design of Figure 7 is shown in Figure 8b.

To get a better feel for the results of Figure 8, Figure 9 shows the detected irradiance pattern of the OPA design at wavelengths of 500 nm, 540 nm, 600 nm and 700 nm. The images are in reverse contrast so that ‘darker’ means ‘brighter’, and are also shown with the orders convolved with a rectangle to increase visibility. The next obvious step is the development of a broadband OPA feedback design algorithm. Even so, considering the change in phase response of the OPA at different electrode periods and operation at wavelengths far from those specified for the AR coatings, the results of both the feedback algorithm and the performance of the OPA as a CTIS disperser are very encouraging.

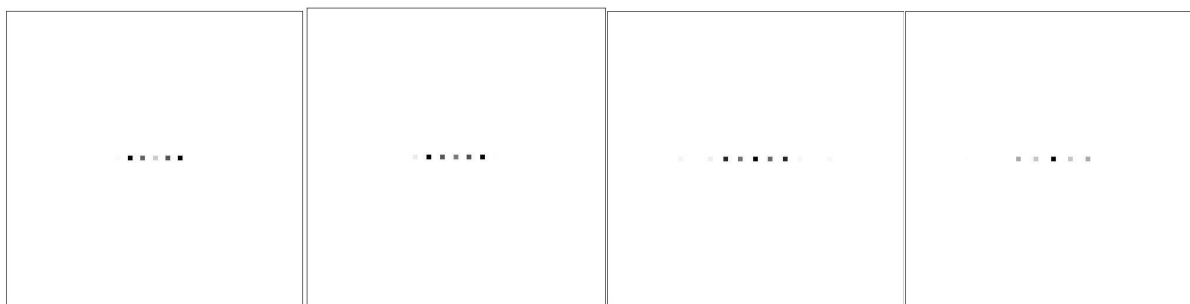


Figure 9: The detected irradiance at wavelengths of 500 nm, 540 nm, 600 nm and 700 nm, from left to right.

4. Conclusion

This work presents the initial progress to date on implementing an electronically tunable LC Optical Phased Array as a CTIS disperser. The overarching goal is to develop the ability to change the CTIS instrument response with no moving parts by changing the disperser period and phase profile. An electronically tunable CTIS disperser allows for the possibility of optical processing to enhance data cube reconstruction quality and reduce data cube reconstruction time.

It is desirable to use current CGH disperser algorithms to design the optimal phase profiles to be programmed to the OPA, but this is not practical because of OPA ‘flyback,’ or inter-phases cross talk. The phase vs. applied voltage curves for the OPA behave as expected for large periods and are obtained via a binary phase experiment. The experiment also shows the radical change in phase response of the OPA for smaller periods because of flyback. For use as a CTIS disperser, a feedback algorithm is necessary to obtain the desired far-field irradiance. Simulated annealing has proven effective as a monochromatic CGH design algorithm with the OPA.

5. Future Work

The next step is the development of a feedback CGH design algorithm to optimize the OPA’s broadband performance. Simulated annealing could again be used as a CGH design algorithm for a polychromatic design using a multi-wavelength squared error merit function. What has been done so far to this end is to take a 32000 iteration design, as presented above, as the initial profile and reduce the iterations to an average of 100 changes per OPA electrode (3200 iterations total) at five different wavelengths. Results have not yielded a satisfactory design so far because the reduction in iterations is too great. The design time of simulated annealing, as it approaches ‘days’ instead of ‘hours,’ becomes a problem as does wear on the grating monochromator which has to rotate a precision turret hundreds to thousands of times for a broadband algorithm to work.

Another option for broadband design is to adapt the current CGH polychromatic algorithms for use with the OPA. This would reduce the number of iterations needed to arrive at a satisfactory broadband solution by at least a factor of 10. The algorithm is not nearly as straightforward as simulated annealing, especially when implemented with the OPA.

Acknowledgments

This work was funded by Defense Advanced Research Projects (DARPA) Grant #DAAD10-02-1-0265 awarded by John C. Carrano. The Optical Phased Array was provided by Dr. Terry Dorschner of Raytheon Network Centric Systems in Lexington, MA, and thanks go out to Dr. Dorschner also for his technical advice and encouragement. The programming of the OPA would not have been possible without the help of Dr. Kevin McNeill of Electrical and Computer Engineering at the University of Arizona. Thanks also to Dr. Daniel Wilson of JPL in Pasadena, CA, for providing yet another set of high quality PMMA CGHs.

References

1. A.F.H Goetz, "Imaging spectrometry for earth remote sensing," *Science*, **228**, No. 4704, pp. 1147-1153 (1985)
2. R.W. Basedow, D.C. Carmer, and M.E. Anderson, "HYDICE system, implementation, and performance," in *Imaging Spectrometry*, M.R. Descour, J.M. Mooney, D.L. Perry, and L.R.B. Illing, eds., Proc SPIE **2480**, 258-267 (1995)
3. W.M. Porter and H.T. Enmark, "A system overview of the Airborne Visible/Infrared Imaging Spectrometer (A VIRIS)," in *Imaging Spectroscopy II*, G. Vane, ed., Proc. SPIE **834**, 22-31 (1985)
4. M.R. Descour and E.L. Dereniak, "Computed-tomography imaging spectrometer: experimental calibration and reconstruction results," *App. Optics*, **34**, No. 22, pp. 4817-4826 (1995)
5. T. Okamoto and I. Yamaguchi, "Simultaneous acquisition of spectral image information," *Opt. Lett.* **16**, 1277-1279 (1991)
6. T. Okamoto, A. Takahashi, and I. Yamaguchi, "Simultaneous acquisition of spectral and spatial intensity distribution," *Appl. Spectrosc.* **47**, 1198-1202 (1993)
7. F.V. Bulygin, G.N. Vishnyakov, G.G. Levin, and D.V. Karpukhin, "Spectrotomography - a new method of obtaining spectrograms of 2-D objects," *Opt. Spectrosc. (USSR)* **71**, 561-563 (1991)
8. M.R. Descour, "Non-Scanning Imaging Spectrometry," Ph.D. dissertation (University of Arizona, Tucson, Ariz., 1994)
9. M.I. Sezan and H. Stark, "Applications of convex projection theory to image recovery in tomography and related areas," in *Image Recovery: Theory and Application*, H. Stark, ed. (Academic, San Diego, Calif., 1987), pp. 415-462
10. P.A. Bernhardt, "Direct reconstruction methods for hyperspectral imaging with rotational spectrotomography," *J. Opt. Soc. Am. A* **12**, 1884-1901 (1995)
11. C.E. Volin, "Portable Snapshot Infrared Imaging Spectrometer," Ph.D. dissertation (University of Arizona, Tucson, Ariz., 2000)
12. P.F. McManamon, T.A. Dorschner, D.L. Corkum, L.J. Friedman, D.S. Hobbs, M. Holz, S. Liberman, N.Q. Nguyen, D.P. Resler, R.C. Sharp, E.A. Watson, "Optical Phased Array Technology," *Proc. IEEE* **84**, pp. 268-298, 1996.
13. C.E. Volin, M.R. Descour, E.L. Dereniak, "Design of broadband-optimized computer-generated hologram dispersers for the computed-tomography imaging spectrometer," in *Imaging Spectrometry VII*, M.R. Descour, Sylvia S. Shen; Eds., Proc. SPIE 4480, 377-387 (Jan 2002)
14. C.L. Coleman, "Computer Generated Holograms for Free-Space Optical Interconnects," Ph.D. dissertation (University of Arizona, Tucson, Ariz., 1998)